

Cite as: H. Shen *et al.*, *Science* 10.1126/science.aal4326 (2017).

Structure of a eukaryotic voltage-gated sodium channel at near-atomic resolution

Huaizong Shen,^{1,2*} Qiang Zhou,^{1,2,3*} Xiaojing Pan,^{1,2*} Zhangqiang Li,^{1,2,3*} Jianping Wu,^{1,2,3*} Nieng Yan^{1,2,3†}

¹State Key Laboratory of Membrane Biology, Tsinghua University, Beijing 100084, China. ²Beijing Advanced Innovation Center for Structural Biology, Tsinghua University, Beijing 100084, China. ³Tsinghua-Peking Joint Center for Life Sciences, School of Life Sciences and School of Medicine, Tsinghua University, Beijing 100084, China.

*These authors contributed equally to this work.

†Corresponding author. Email: nyan@tsinghua.edu.cn

Voltage-gated sodium (Na_v) channels are responsible for the initiation and propagation of action potentials. They are associated with a variety of channelopathies and are targeted by multiple pharmaceutical drugs and natural toxins. Here, we report the cryo-EM structure of a putative Na_v channel from American cockroach (designated Na_vPaS) at 3.8-Å resolution. The voltage sensing domains (VSDs) of the four repeats exhibit distinct conformations. The entrance to the asymmetric selectivity filter vestibule is guarded by heavily glycosylated and disulfide bond-stabilized extracellular loops. On the cytoplasmic side, a conserved amino terminal domain is placed below VSD_I and a carboxy terminal domain binds to the III-IV linker. The structure of Na_vPaS establishes an important foundation for understanding function and disease mechanism of Na_v and related Ca_v channels.

Voltage-gated sodium (Na_v) channels are ubiquitously present in eukaryotes and responsible for the initiation of electrical signaling in excitable systems such as nerve and muscle. The Na_v channels remain closed at resting potentials and activate upon membrane depolarization, allowing for the Na^+ influx that corresponds to the rapid upstroke of an action potential. Na_v channels inactivate rapidly; meanwhile, the activation of voltage-gated potassium (K_v) channels resets the membrane electric field to resting state. Defects in Na_v channels underlie a variety of neurological and cardiovascular disorders. Over 1,000 mutations have been identified in human Na_v channels that are associated with epilepsy, arrhythmia, muscle paralysis, chronic pain, and other syndromes (1–5). Na_v channels are targeted by multiple toxins and pharmaceutical drugs (6, 7).

The eukaryotic Na_v channels consist of a pore-forming α subunit and auxiliary β subunits (8). The α subunit is sufficient for voltage-dependent ion conductance, while the β subunits facilitate membrane localization and modulate channel properties (9). There are 9 isoforms of Na_v α subunits in human, designated $\text{Na}_v1.1\text{-Na}_v1.9$ (10). A sequence related protein, now named Na_vX , was found to function in salt sensing (11). The α subunit, similar to the closely related Ca_v channels (12), is comprised of a single polypeptide chain that folds to four homologous repeats (domains I–IV) each containing six transmembrane segments S1–S6 (Fig. 1A). The four sets of S5 and S6 segments and their intervening sequences enclose the ion permeation pore domain, while the S1–S4 segments in each repeat form a voltage sensing domain (VSD) (13). The α subunit is subjected to multiple

posttranslational modifications such as glycosylation, phosphorylation, and palmitylation (14). Na_v channels have also been found in bacteria, exemplified by NaChBac (15). Similar to K_v channels, bacterial Na_v channels are tetramers of four identical subunits

The ion selectivity of a voltage gated ion channel is determined by the selectivity filter (SF), a molecular sieve enclosed by the partial membrane penetration loops between S5 and S6 segments (16–18). The residues that determine ion selectivity are identical in each protomer in the homotetrameric bacterial channels (15, 19) and in the four homologous repeats of eukaryotic Ca_v channels (20, 21). In contrast, a different residue, Asp/Glu/Lys/Ala (DEKA), is present at the corresponding SF locus in each repeat of eukaryotic Na_v channels (22, 23) (Fig. 1A).

The eukaryotic Na_v channels can undergo rapid voltage-dependent transitions between closed and open states, a prerequisite for producing the regenerative wave of electrical signals. The inner tetrahedral bundle of the pore domain screws at the cytoplasmic boundary of the membrane, forming the intracellular activation gate. Essential for voltage gating, VSDs contain the “gating charges” (24), which are a set of highly conserved positively charged residues occurring at every third place along S4 segment. Upon depolarization, according to measurements in K_v channels, approximately 12 gating charges per channel are transferred across the membrane from the intracellular side to the extracellular side (25–27). During this process, the gating charges interact sequentially with conserved acidic or polar residues on S2 (designated An1 and An2) and S3 segments

(28–30). A charge transfer center consisting of An2 and a cyclic hydrophobic residue on S2 and an adjacent Asp on S3 was identified that facilitates charge transfer (31).

While multiple models of voltage-dependent activation have been proposed, the precise mechanism remains to be elucidated. It is generally accepted that the S4-S5 linker helices translate the voltage-dependent shifts of S4 segments to pore opening in voltage-gated ion channels with the “canonical” domain swapped arrangement (32). However, the S4-S5 helices are missing in the recently resolved structures of Eag1, Slo1, HCN1, and CNG channels whose domains are not swapped, suggesting potentially different electromechanical coupling mechanism for these channels (33–36).

While the activation mechanism has not been fully understood, at least as bewildering are the intricate inactivation mechanisms for voltage-gated channels. Fast inactivation, which takes place on millisecond scale, is executed by a cytoplasmic moiety between repeats III and IV of Na_v channels (37). During prolonged depolarization, slow inactivation takes place by a mechanism that is not well understood (38), although it is thought at least in some cases that a conformational change of the selectivity filter underlies this process in Na_v and K_v channels (39–43).

Detailed atomic model of a eukaryotic Na_v channel is required to reveal the molecular basis for ion selectivity, voltage-dependent activation and inactivation, as well as recognition of toxins, agonists and inhibitors. Previous structural interpretation of Na_v channels have been mostly based on the crystal structures of K_v channels and then on the bacterial Na_v channels (17, 30, 32, 44, 45). The technological breakthrough in electron microscopy (EM) has offered unprecedented opportunity for structure elucidation at near atomic resolutions of macromolecules that were challenging by X-ray crystallography (46–48). The recent structural elucidation of the $\text{Ca}_{v1.1}$ channel complex provides a more relevant template for homology modeling of Na_v channels (49, 50).

The bottleneck for structural determination of a eukaryotic Na_v channel exists in the generation of sufficient amount of high-quality proteins (51). Unsuccessful in obtaining homogeneous proteins from either electric eel or mammalian Na_v channel preparations, we turned to insect Na_v channels (52). Similar to their mammalian relatives, the insect Na_v channels have single-chain α subunit and auxiliary subunit exemplified by TipE (53). Among the insect homologs tested, we succeeded in purifying sufficient recombinant proteins for a putative Na_v channel from the American cockroach *Periplaneta americana* (54). To facilitate description, the protein that was originally named PaFPC1 is designated Na_vPaS . Here we report the structure of Na_vPaS at a nominal resolution of 3.8 Å determined using single-particle cryo-EM.

Results

Structural determination of Na_vPaS

Na_vPaS shares 36–43% sequence identities with human $\text{Na}_v1.1\text{-}1.9$, containing the signature DEKA residues on the selectivity filter and highly conserved transmembrane segments (fig. S1). The variations mainly exist in the intracellular linkers between repeats. Na_vPaS , consisting of 1553 amino acid residues, has considerably shorter I-II and II-III linkers than the mammalian and other insect homologs, whose sequence lengths range between 1800 to 2050 residues. The III-IV linker of Na_vPaS is of identical length with those of the human channels, but lacks the Ile/Phe/Met/Thr (IFMT) or similar motif that is critical for fast inactivation (55) (fig. S1).

The electrophysiological properties of Na_vPaS have not been characterized. We attempted to record Na_vPaS in several expression systems, including HEK293 cells, Chinese hamster ovary cells, and *Xenopus laevis* oocytes, in the presence or absence of the β subunits PaTipE and PaTEH1 (56, 57). Despite that the channel can be expressed on plasma membrane even in the absence of any β subunit (fig. S2A), no Na^+ current could be unambiguously assigned to Na_vPaS in all three tested systems, a problem that is occasionally encountered for heterologously expressed channels (30, 56). While the physiological function and biophysical properties of Na_vPaS remain to be investigated, it possesses all the hallmarks of a Na_v channel except for the fast inactivation motif and displays good solution behavior (figs. S1 and S2B). We thereby proceeded with structural determination using cryo-EM.

Details of grid preparation, cryo-EM data acquisition, and structural determination of Na_vPaS are presented in Supplemental Methods (Fig. 1, B and C, and figs. S2 and S3). We selected 1.3 million particles and calculated an EM map to 3.8 Å according to the gold-standard Fourier shell correlation (FSC) 0.143 criterion (Fig. 1, C and D, and figs. S2, C to G). The EM maps are well resolved for most of the extracellular and transmembrane sequences (figs. S4 and S5). In total 1323 residues are structurally modeled with 1177 side chains assigned, covering the complete voltage-gated ion channel fold, extracellular loops of the pore domain, the intact III-IV linker, and the carboxy terminal domain (CTD). A poly-Ala backbone was built for the amino terminal domain (NTD) containing residues 47–120 that immediately precede the VSD of repeat I (VSD_I).

The missing segments are all on the intracellular side, including the N-terminal 46 amino acids, the I-II linker (residues 436–501) and II-III linker (residues 747–832), and the C-terminal 32 residues. In addition to the polypeptide chain, 20 sugar moieties are built into 7 glycosylation sites on the extracellular loops, namely the L5 loops between S5 and P1 segments and the L6 loops between P2 and S6 segments

(Fig. 1D and table S1).

The overall structure resembles that of the $\alpha 1$ subunit of the rabbit $\text{Ca}_v 1.1$ (49). The sequence for NTD, which is located below VSD_I and between VSD_I and S6_I, is conserved in Na_v channels and harbors a number of disease-related mutations (50) (Fig. 1D and figs. S1 and S6). We will refrain from detailed analysis of NTD due to the low resolution for this domain (fig. S2F).

The asymmetric selectivity filter

In Na_vPaS , the SF vestibule is enclosed by the side groups of the signature residues Asp375/Glu701/Lys1061/Ala1353 at the upper position and the carbonyl oxygen atoms of the two preceding residues in each repeat at lower level (Fig. 2, A and B). Above DEKA, the outer negative ring composed of Glu378/Glu704/Gln1065/Asp1356 guards the entrance to the SF vestibule. In human Na_v channels, a conserved Asp in repeat III occupies the position corresponding to Gln1065 (Fig. 2A and fig. S1). In EM reconstructions, the densities for the carboxylate groups of Asp and Glu residues are usually invisible due to radiation damage. Fortunately, the backbone and the alkyl groups are discernible for most of the negatively charged residues in SF and the P1 and P2 helices of Na_vPaS (fig. S5, A and B).

The SF vestibule of a bacterial Na_v channel is also composed of side groups for the outer site and eight carbonyl oxygen atoms for the inner site (17, 30, 45). However, the SF vestibule of the eukaryotic Na_v channel is distinct from that of the bacterial counterparts with respect to both chemical composition and structural conformation, providing the molecular basis to investigate the different selectivity mechanisms between eukaryotic and bacterial Na_v channels (58) (Fig. 2C). The SF sequence in repeat II is one residue shorter than in the other three repeats. Consistently, the backbone conformation of SF_{II} deviates from the other three, further adding to the asymmetry of the SF vestibule (Fig. 2D and fig. S1).

At current resolution, we refrain from assessment of the precise dimension of the SF vestibule (59) or analysis of the interactions between D/E and K. Nevertheless, the side group of Lys1061 appears to adopt a downward conformation with the amino group pointing away from Asp375 and Glu701 (Fig. 2B and fig. S5, B and C). The protein for data acquisition was prepared in the presence of 50 mM NaCl. Discontinuous densities are observed in the SF vestibule. However, the relatively weak signal and the slight positional variations between half maps make it difficult to distinguish between the densities of Na^+ ions and noises (fig. S5B).

A closed pore with one small fenestration

The pore domain of Na_vPaS is well resolved in the EM re-

construction, allowing accurate assignment of side groups (Fig. 3A and figs. S4 and S5). Unexpectedly, the complete extracellular L5 and L6 loops are also resolved, suggesting their structural stability even in the absence of binding partners. Indeed, four pairs of disulfide bonds are identified within the L5_I, L5_{III}, and L6_{IV} loops. An additional disulfide bond is found between the P2 helix and S6 in Repeat II (Fig. 3A and fig. S7A). All these disulfide-forming Cys residues are invariant in the human and insect Na_v channels (fig. S1).

The L5 loops in Repeats I and III are particularly long, containing short helices and anti-parallel β -strands. These bulky extracellular structures provide the scaffold for binding with the auxiliary β subunits through covalent or non-covalent interactions (9). A recent characterization identified Cys910 in h $\text{Na}_v 1.2$, a residue on the L5_{II} loop, to be disulfide-bonded with the $\beta 2$ subunit (60). Despite that the specific Cys is not conserved in Na_vPaS , the similar length and general sequence conservation of L5_{II} loop between Na_vPaS and human Na_v channels will facilitate structural modeling of complex formation between α and β subunits of Na_v channels (figs. S1 and S6).

Compared to the extracellular loops in $\text{Ca}_v 1.1$ that are involved in the interactions with the $\alpha 2\delta$ subunit (18, 49), the L5 and L6 loops of Na_vPaS have more folded secondary structural elements and are heavily glycosylated (Fig. 3, A and B, and fig. S7A). The extracellular loops of Na_vPaS leave a spacious opening to the outer mouth of the SF vestibule. The surfaces above SF are enriched in negatively charged residues distributed on the L5 loops in Repeats I-III and the L6_{IV} loop, a structural shield that would attract cations and exclude anions (Fig. 3B).

The S6 tetrahedral bundle encloses a distinctive permeation path that is sealed at the intracellular boundary by two layers of hydrophobic residues Leu, Ile, Val, and Ala (Fig. 3C). Interestingly, the central cavity between the SF vestibule and the intracellular gate appears to have a smaller volume than that of $\text{Ca}_v 1.1$ (49). In particular, a number of polar and charged residues line up the wall of the central cavity, including the highly conserved Asn residue (Asn409/Asn729/Lys1105/Asn1404) on each S6 segment (Fig. 3D and fig. S7B).

Similar to $\text{Ca}_v 1.1$, the four-fold pseudosymmetry of the pore domain is disrupted by the conformational variations of the S5 and S6 segments (fig. S7C). Unexpectedly, only one small pore fenestration is observed on the side constituted by repeats III and IV whereas the other three sides are completely sealed from the lipid bilayer, a conformational state that differs from the structures of prokaryotic Na_v channels and $\text{Ca}_v 1.1$, wherein pore fenestrations are present on all four sides (17, 30, 45, 49) (Fig. 3E and fig. S7D).

The III-IV linker and CTD

Another important functional element revealed by the Na_vPaS structure is the III-IV linker and the CTD, which interact with each other below repeat IV, reminiscent of the Ca_v1.1 structure (49) (Figs. 1D and 4A). The III-IV linker is involved in the fast inactivation gating of Na_v channels, with the hydrophobic cluster IFM being a critical motif (55, 61–63). The solution structure of an isolated III-IV linker and the cryo-EM structure of Ca_v1.1 both revealed the presence of a short α helix presumably following the IFM motif (49, 64). However, the residues corresponding to IFM are missing in Ca_v1.1, preventing modeling of this motif in the context of the overall structure.

In the reconstruction of Na_vPaS, the complete III-IV linker is resolved, comprising a helix followed by a long unwound segment (Fig. 4, A and B). The IFM-corresponding residues are ₁₁₂₇Ala/Thr/Asp₁₁₂₉ (ATD) in Na_vPaS, which are located at a short turn connecting the C terminus of S6_{III} and the III-IV helix (Fig. 4B). In the side view, the ATD and the following III-IV helix are sandwiched between the C-terminal tips of S6_{III} and S6_{IV}, with the ATD motif at similar height to the C-termini of S6_{III} and S6_{IV}, approximately 15 Å away from the lower level of the intracellular gate (Fig. 4B). Because the adjacent structural elements, including S4-S5_{IV}, S6_{III}, S6_{IV}, and CTD, are conserved between Na_vPaS and human Na_v channels, the position of ATD may reflect those of the corresponding IFM in the human Na_v channels (fig. S1). The structure implies that the short linker between the C terminus of S6_{III} and the IFM motif may impede the latter from reaching the intracellular gate unless S6_{III} and S6_{IV} undergo a pronounced conformational rearrangement. Notwithstanding the structural analysis, it remains to be characterized whether Na_vPaS undergoes fast inactivation.

The polar interactions along the intracellular surface of repeat IV are extensive, involving the III-IV linker, CTD, VSD_{IV}, S4-S5_{IV}, S6_{IV} and S6_{III} (Fig. 4C). In addition to the contacts with CTD, the III-IV linker also binds to some cytoplasm-facing residues in VSD_{IV}, S6_{IV} and S6_{III}. The first α -helix of CTD interacts with VSD_{IV} and S4-S5_{IV} (Fig. 4, C and D). The structure of Na_vPaS-CTD is nearly identical to that of the Na_v1.5-CTD (Fig. 4D) (65). The interface residues between CTD and the S4-S5_{IV} linker, exemplified by the three consecutive negatively charged residues on the first α helix of CTD and the repetitively occurring positive residues on the S4-S5_{IV} linker, are highly conserved (Fig. 4C and fig. S1). Therefore, the cytoplasmic interfaces observed in Na_vPaS are likely preserved in the human Na_v channels. The extensive interactions among the functional elements including VSD_{IV}, S4-S5_{IV}, S6_{III}, S6_{IV}, III-IV linker and CTD provide a molecular foundation to interpret the critical role of VSD_{IV} in inactivation in the recently proposed “asynchronous gating model” (4, 66–68) and the involvement of CTD in inacti-

vation (69, 70).

The voltage sensing domains in distinct conformations

In the structure of Na_vPaS, the four VSDs including the connecting loops are completely resolved (fig. S4A). Unlike the homotetrameric K_v channels and bacterial Na_v channels, the relative angles between neighboring VSDs of Na_vPaS are all several degrees deviated from 90° (Fig. 5A). The lengths and sequences of VSD_{IV} are similar between Na_vPaS and human Na_v1.7 (fig. S1). However, the S3 and S4 segments in Na_vPaS-VSDs are each one helical turn shorter than those in the chimeric VSD generated by fusing the extracellular halves of VSD_{IV} from Na_v1.7 to the scaffold of Na_vAb (designated as the Na_vAb-1.7 VSD4) (71) (Fig. 5B). The four VSDs have different numbers of gating charge residues (fig. S1). Similar to the numbering system used in Ca_v1.1 (49), we define the Arg/Lys on the last helical turn of the S4 segment as R6. Thereby S4_I and S4_{III} have R2-R5, while S4_{II} and S4_{IV} have R2-R6. The invariant Lys (K1) on S4_{III} in human Na_v channels is replaced by Gln948 in Na_vPaS (fig. S1).

In mammalian Na_v channels, the four repeats display distinct activation kinetics with the molecular basis unclear (67). In the structure of Na_vPaS, the corresponding gating charges are at different positions relative to the charge transfer center (CTC) and An1, with VSD_{II} and VSD_{III} at the most and least activated conformations, respectively, among the four (Fig. 5, C and E).

The S4 segments adopt 3_{10} helical conformations in the VSDs of repeats I-III, while the two extracellular helical turns of S4_{IV} relax to α -helix (Fig. 5D). Only R2 in VSD_{III} is coordinated by An1, while those in the other three VSDs are out of reach of An1. R3 is coordinated by An1 in three VSDs other than VSD_{II}, in which R4 is “up” enough to interact with An1. R5 is similarly coordinated by An2 and the conserved Asp on S3 in VSD_I and VSD_{II}. The C α of R5 in VSD_{IV} is at a further “down” position relative to CTC, but its side chain can still bind to the two CTC negative residues. VSD_{III} represents the least activated one as its R4 is coordinated by the negative residues of CTC below the occluding residue Phe901 (Fig. 5D).

It is noteworthy that the C α atoms of all the gating charges are at similar heights in S4_{III} and S4_{IV}. It is the swing of the long side chain of Arg that places the guanidinium group of R4 below or above the occluding Phe in VSD_{III} and VSD_{IV}, respectively (Fig. 5E). A more pronounced difference involves the backbone shift. The backbone of S4_{III} moves down by one complete helical turn relative to S4_{II} and by half a helical turn in height relative to S4_I when the corresponding VSDs are aligned with respect to CTC and An1 (Fig. 5E). The molecular determinants for the heterogeneous conformations of the VSDs at 0 mV remain to be elucidated.

Structural comparison between Na_vPaS and Ca_v1.1

Among the prokaryotic and eukaryotic Na_v and Ca_v channels whose structures are available, Ca_v1.1 is most closely related to Na_vPaS (fig. S8). Structural comparison of Na_vPaS and Ca_v1.1 reveals similarity in the general structural organization and, more interestingly, pronounced conformational changes of both the pore domain and VSDs (Fig. 6A and Movie 1).

When the structures of Na_vPaS and Ca_v1.1 are overlaid relative to the funnel constituted by the selectivity filter and pore helices (the P1-SF-P2 segments in the corresponding repeats), VSD_{II} and VSD_{IV} of Na_vPaS exhibit a slight clockwise rotation from the corresponding domains of Ca_v1.1 in the intracellular view, while the respective positions of VSD_I and VSD_{III} are similar in the two structures (Fig. 6A).

Despite that both channels are closed at the intracellular gate, the pore domain of Na_vPaS appears to be further tightened by an overall right-handed screw of the S5 and S6 segments as well as the S4-S5 constriction ring around the central axis of the pore domain (Fig. 6A and Movie 1). Similar structural shifts also occur between Na_vPaS and bacterial Na_v channels (fig. S9).

Accompanying the overall twisting of the S6 tetrahedral bundle, each S6 segment undergoes axial rotation starting at the relatively conserved G(S/T)F motif or corresponding positions (Fig. 6B, Movie 2, and figs. S1 and S8). Consequently, the afore-mentioned Asn residues point to the central cavity in Na_vPaS (Fig. 3D), whereas the corresponding ones in Ca_v1.1 are outside the cavity and able to contact residues in the neighboring S4-S5 segment (Fig. 6B, Movie 2, and figs. S1 and S8). Single point mutation of the conserved Asn on S6_I or S6_{III} alters slow inactivation in Na_v1.2 and Na_v1.4 (72–74). The pronounced shifts of the corresponding residues between Na_vPaS and Ca_v1.1 provide a clue to the mechanistic understanding of their involvement in slow inactivation.

The structural comparison between Na_vPaS and Ca_v1.1 suggests a potential mechanism for the gating of the pore domain fenestrations (Figs. 3E and 6C and Movie 3). From Na_vPaS to Ca_v1.1, the S5 and S6 helical bundles are relaxed through the overall iris-like rotation. Accompanying this motion, all the closed pore fenestrations in the structure of Na_vPaS become open (Fig. 6C and Movie 3). The fenestration constituted by S6_{III} and S6_{IV} was suggested to be the receptor site for local anesthetic drugs, involving Phe1764 and Tyr1771 in Na_v1.2 and Phe1579 in Na_v1.4 (75, 76). The corresponding residue for Na_v1.2-Phe1764 and Na_v1.4-Phe1579 is Cys1399 in Na_vPaS, which sits on one side of the fenestration (Fig. 6C, inset). Tyr1406, which corresponds to Tyr1771 in Na_v1.2, is on the opposite side of the fenestration in the structure of Na_vPaS, but encloses the fenestration in the conformation of Ca_v1.1 owing to the axial rotation of S6_{IV}

(Fig. 6C, inset, and Movie 3). These structural observations may facilitate mechanistic elucidation of the state-dependent action of local anesthetics targeting Na_v channels.

Discussion

Despite that Na_vPaS and Ca_v1.1 are both captured at closed conformations and their functional states are yet to be defined, the concerted conformational shifts of pore domain elements and VSDs between the two structures may shed light on the understanding of electromechanical coupling mechanism of voltage-gated ion channels (Fig. 7 and Movies 4 and 5).

In the cryo-EM structure of Ca_v1.1, all four VSDs display similar conformations with R5 coordinated by CTC and R4 close to An1 (49), a state reminiscent of Na_vPaS-VSD_{II}. Therefore, VSDs I, III, and IV in Ca_v1.1 appear to be more activated than the corresponding ones in Na_vPaS (Fig. 5, D and E). From Na_vPaS to Ca_v1.1, the S4 segments in these three VSDs indeed display a tilting motion, which is a combination of upward shift of the helix and outward displacement of the intracellular tip of S4 from the central axis (Fig. 7A and Movie 4). The ensuing S4-S5 segments are pulled outward by the S4 segments accordingly. Due to the tight connection between S4-S5 segment and the ensuing S5 segment, any shift of S4-S5 can be immediately translated to S5 in the same repeat.

The coupled motions between VSDs and pore domain are more evident for VSD_I and VSD_{III} and their respective neighboring pore domain segments (Movie 4). S5_{II} and S5_{IV} appear to undergo concerted shifts with S4_I and S4_{III}, respectively, as the involved interfaces are largely preserved in Na_vPaS and Ca_v1.1 (Fig. 7A and Movie 4). The neighboring S4-triggered shift of a S5 segment may in turn drag its preceding S4-S5 segment to move accordingly. The motion of one S4-S5 segment would then be coupled to the neighboring S4-S5, S5 and S6 segments. The conformation and position of S6 can also be affected by both S5 in the same repeat and S6 from the neighboring repeat (Fig. 7B). To be brief, the electromechanical coupling of a voltage-gated ion channel, which is like a delicate gear, may involve extraordinarily intricate interactions among S4-S5, S5, and S6 segments in the same repeat and between neighboring repeats and subsequent re-arrangement of these interactions once the motion is triggered by the voltage-dependent conformational shifts of VSDs (Fig. 7B).

More than 1,000 disease-associated mutations have been identified in human Na_v channels (50). It is known that the selectivity filter, gating charge residues, and the III-IV linker are hotspots for disease mutations, while the disease-causing mechanism for the majority of the mutations remains enigmatic. The structure of Na_vPaS provides a tem-

plate to map hundreds of disease mutations and serves as a framework to mechanistically investigate these mutations (fig. S10). For instance, a number of mutations are mapped to the interfaces between S4 and S5 of neighboring repeats. Alteration of the interface residues may affect electromechanical coupling as analyzed above (Fig. 7, B and C, and Movie 5).

Conclusions

The near atomic resolution structure of a single-chain eukaryotic Na_v channel establishes an important foundation for investigating the function and disease mechanisms of Na_v channels and for structure-guided drug development. Despite the exciting features revealed by the structure, many important questions remain to be answered. The Na^+ selectivity cannot be explained by a single structure, especially in the absence of the bound Na^+ in the SF vestibule. The near atomic resolution structure of Na_vPaS provides the template for molecular dynamics simulations analysis. The conformational changes between Na_vPaS and $\text{Ca}_{v,1.1}$ may shed light on the molecular understanding of electromechanical coupling mechanism of Na_v and Ca_v channels. Nonetheless, we have to interpret the conformational changes with caution because the comparison is made for two channels with considerable sequence variations and the functional states of the structures are yet to be defined. A series of structures of the same channel in distinct states are required to establish the structure-function correlation. The technological advances of cryo-EM and a protein that can be conveniently manipulated will make this premise possible.

Materials and methods

Transient expression of Na_vPaS

The optimized coding DNA for Na_vPaS (Uniprot: D0E0C2) with Twin-Strep-tag and FLAG tag in tandem at the amino terminus was cloned into the pCAG vector (77). HEK293F cells (Invitrogen) were cultured in SMM 293T-I medium (Sino Biological Inc.) under 5% CO_2 in a Multitron-Pro shaker (Infors, 130 r.p.m.) at 37°C. When the cell density reached 4×10^6 cells per ml, the plasmid was transfected. For one liter cell culture, 3 mg plasmids were pre-incubated with 6 mg 25-kDa linear polyethylenimines (PEIs) (Polysciences) in 25 ml fresh medium for 15–30 min. The transfection was initiated by adding the mixture into cell culture, followed by dilution of the cell culture to 2×10^6 cells per ml with fresh medium. Transfected cells were cultured for 48 hours before harvesting. The expression of target protein was examined by Western blot using monoclonal antibodies against the FLAG tag.

Immunostaining of HEK293 cells expressing Na_vPaS

HEK293 cells, cultured on poly-L-ornithine (Sigma)-coated

15 mm circular coverslips seated in 35 mm dishes, were co-transfected with the expression plasmid for Na_vPaS and an eGFP-coding plasmid when cell confluence reached 30–50%. After incubation at 37°C under 5% CO_2 for 36 hours, the transfected cells were washed three times with PBS (Gibco) before being fixed by 4% paraformaldehyde (Electron Microscopy Sciences) in PBS at room temperature for 15 min. Rinsed twice, the cells were then blocked by 4% BSA (Sigma) in PBS plus 0.5% (w/v) Triton X-100 (PBS-TX) (Invitrogen) for one hour before the 4% BSA was replaced by anti-Strep-tag primary antibody (Biocompare). After incubation at 4°C overnight, the cells were washed three times with PBS-TX before treated with the goat anti-mouse IgG highly cross-adsorbed secondary antibody, Alexa Fluor 568 (Invitrogen) and phalloidin, Alexa Fluor 647 (Invitrogen). After being incubated at 22°C for two hours, the cells were washed three times with PBS-TX. The coverslips were covered by a layer of DABCO (Sigma) and sealed on an object slide by transparent nail polish. The sample was imaged under microscope LSM780 (Zeiss).

Purification of the Na_vPaS protein

For each batch of protein purification, eight liters of transfected HEK293F were harvested by centrifugation at 800 g and resuspended in lysis buffer containing 25 mM Tris-HCl, pH 7.4, and 50 mM NaCl. The suspension was supplemented with 1% (w/v) digitonin (Sigma), and protease inhibitor cocktail containing 2 mM phenylmethylsulfonyl fluoride (PMSF), 2.6 $\mu\text{g}/\text{ml}$ aprotinin, 1.4 $\mu\text{g}/\text{ml}$ pepstatin, and 10 $\mu\text{g}/\text{ml}$ leupeptin, and incubated at 4°C for 2 hours. After ultra-centrifugation at 200,000 g for 25 min, the supernatant was applied to anti-Flag M2 affinity gel (Sigma) and flowed through by gravity at 4°C. The resin was rinsed three times with the wash buffer containing 25 mM Tris-HCl, pH 7.4, 50 mM NaCl, 0.1% digitonin (Sigma), and protease inhibitor cocktail. The target Na_vPaS protein was eluted with wash buffer plus 200 $\mu\text{g}/\text{ml}$ FLAG peptide (Sigma). The eluent was then applied to the Strep-Tactin Sepharose (IBA) and flowed through by gravity. The resin was rinsed three times with the aforementioned wash buffer. The protein was eluted with the wash buffer plus 2.5 mM D-Desthiobiotin (IBA). The eluent was then concentrated using a 100-kDa cut-off Centricon (Millipore) and further purified by size exclusion chromatography (Superose-6, GE Healthcare). The peak fractions were pooled and concentrated to 50 μl at a concentration of approximately 1 mg/ml.

Cryo-EM data acquisition

Cryo-EM grids were prepared with Vitrobot Mark IV (FEI). Aliquots (3.5 μl) of freshly purified Na_vPaS were placed on glow-discharged holey carbon grids (Quantifoil Cu R1.2/1.3). Grids were blotted for 3.5 s and flash-frozen in liquid ethane

cooled by liquid nitrogen. A total of 13,757 movie stacks were semi-automatically collected with UCSF Image4 in super-resolution mode on Titan Krios operating at 300 kV and equipped with Gatan K2 Summit detector at a nominal magnification of 22,500 X. The defocus range was set from -1.7 μ m to -2.6 μ m. Each stack was exposed for 8 s with an exposing time of 0.25 s per frame, resulting in a total of 32 frames per stack. The total dose rate was about 50 e/ \AA^2 for each stack. The stacks were first motion corrected with MotionCorr (78) and binned 2 fold, resulting in a pixel size of 1.307 \AA /pixel. The output stacks from MotionCorr were further motion corrected with MotionCor2 (79), meanwhile dose weighting was performed (80). The defocus values were estimated with Gctf (81).

Image processing

A diagram of the procedures for data processing is presented in fig. S3. A total of 11,843 good micrographs were manually selected, from which a total of 4,739,175 particles were automatically picked using RELION 1.4 (82–84) or 2.0 (85). After 2D classification with RELION 1.4 or 2.0, a total of 3,039,806 good particles were selected and subjected to global angular search 3D classification using RELION 2.0 with one class and step size of 7.5°. The trans-membrane domain and CTD of Ca_v1.1 α 1 that was low-pass filtered to 60 \AA was used as the initial model. After global angular search 3D classification, the particles were further subjected to 3D classification with 3 to 10 classes and local angular search step of 3.75°. The local angular search 3D classification was performed for several times, with the output from different iterations of the global angular search 3D classification as input. A total of 1,962,964 good particles from the local angular search 3D classification were combined and re-extracted from the magnification distortion corrected micrographs (86). The pixel size after magnification distortion correction is 1.295 \AA /pixel. A total of 1,958,925 non-outlier particles were subjected to several cycles of random-phase 3D classification (87) to remove bad particles. The handedness of the 3D reconstruction was checked and corrected. The particles selected from random-phase 3D classification were subjected to 3D auto-refinement with RELION 2.0. The final particle number for the 3D auto-refinement is 1,373,581. The resolution was estimated with the gold-standard Fourier shell correlation 0.143 criterion (88) with high resolution noise substitution method (89).

Model building and structure refinement

The 3.8 \AA reconstruction map was used for model building. The structure of Ca_v1.1 α 1 was used as the starting model (PDB code: 5GJV, chain A), fitted into the EM map by CHIMERA. CHAINSAW (90) was used to keep the side chains of the conserved residues and to remove the non-

conserved side chains based on the sequence alignment between Ca_v1.1 and Na_vPaS. Model building was performed in COOT (91). The assignment of the four repeats was based on the extracellular loops and the CTD. De novo model building was then performed for each repeat. Sequence assignment was guided mainly by bulky residues. The chemical properties of amino acids were considered during model building. The model building of the CTD was facilitated by docking of the crystal structures of CTDs of Na_v1.2 and Na_v1.5 (PDB codes: 4JPZ and 4DCK, respectively). After these assignments, a globular density near the intracellular side of VSD_I remained to be modeled. Backbone trace suggested that it should belong to the NTD. A poly Ala model was built for this domain due to insufficient resolution for side chain assignment.

Structure refinement was performed using phenix.real_space_refine application in PHENIX (92) in real space with secondary structure and geometry restraints to prevent structure over-fitting. The final model was refined against the 3.8 \AA map using REFMAC (93) in reciprocal space, using secondary structure restraints that were generated by ProSMART (94). Overfitting of the overall model was monitored by refining the model in one of the two independent maps from the gold-standard refinement approach and testing the refined model against the other map (95) (fig. S2D). Statistics of the 3D reconstruction and model refinement can be found in table S1.

For structural analysis, the conserved residues between human Na_v1.4 and Na_vPaS were mapped to the structure of Na_vPaS using ConSurf (96).

REFERENCES AND NOTES

1. A. L. Hodgkin, A. F. Huxley, Resting and action potentials in single nerve fibres. *J. Physiol.* **104**, 176–195 (1945). doi:10.1113/jphysiol.1945.sp004114 Medline
2. A. L. Hodgkin, A. F. Huxley, A quantitative description of membrane current and its application to conduction and excitation in nerve. *J. Physiol.* **117**, 500–544 (1952). doi:10.1113/jphysiol.1952.sp004764 Medline
3. B. Hille, *Ion Channels of Excitable Membranes* (Sinauer Associates, Sunderland, MA, ed. 3, 2001).
4. C. A. Ahern, J. Payandeh, F. Bosmans, B. Chanda, The hitchhiker's guide to the voltage-gated sodium channel galaxy. *J. Gen. Physiol.* **147**, 1–24 (2016). doi:10.1085/jgp.20151492 Medline
5. W. A. Catterall, Sodium channels, inherited epilepsy, and antiepileptic drugs. *Annu. Rev. Pharmacol. Toxicol.* **54**, 317–338 (2014). doi:10.1146/annurev-pharmtox-011112-140232 Medline
6. S. S. Pineda, E. A. Undheim, D. B. Rupasinghe, M. P. Ikonomopoulou, G. F. King, Spider venomics: Implications for drug discovery. *Future Med. Chem.* **6**, 1699–1714 (2014). doi:10.4155/fmc.14.103 Medline
7. S. K. Bagal, B. E. Marron, R. M. Owen, R. I. Storer, N. A. Swain, Voltage gated sodium channels as drug discovery targets. *Channels (Austin)* **9**, 360–366 (2015). doi:10.1080/19336950.2015.1079674 Medline
8. W. A. Catterall, The molecular basis of neuronal excitability. *Science* **223**, 653–661 (1984). doi:10.1126/science.6320365 Medline
9. H. A. O'Malley, L. L. Isom, Sodium channel β subunits: Emerging targets in channelopathies. *Annu. Rev. Physiol.* **77**, 481–504 (2015). doi:10.1146/annurev-physiol-021014-071846 Medline
10. A. L. Goldin, R. L. Barchi, J. H. Caldwell, F. Hofmann, J. R. Howe, J. C. Hunter, R. G.

- Kallen, G. Mandel, M. H. Meisler, Y. B. Netter, M. Noda, M. M. Tamkun, S. G. Waxman, J. N. Wood, W. A. Catterall, Nomenclature of voltage-gated sodium channels. *Neuron* **28**, 365–368 (2000). doi:10.1016/S0896-6273(00)00116-1 Medline
11. E. Watanabe, A. Fujikawa, H. Matsunaga, Y. Yasoshima, N. Sako, T. Yamamoto, C. Saegusa, M. Noda, Nav2/NaG channel is involved in control of salt-intake behavior in the CNS. *J. Neurosci.* **20**, 7743–7751 (2000). Medline
12. M. Strong, K. G. Chandy, G. A. Gutman, Molecular evolution of voltage-sensitive ion channel genes: On the origins of electrical excitability. *Mol. Biol. Evol.* **10**, 221–242 (1993). Medline
13. Y. Jiang, A. Lee, J. Chen, V. Ruta, M. Cadene, B. T. Chait, R. MacKinnon, X-ray structure of a voltage-dependent K⁺ channel. *Nature* **423**, 33–41 (2003). doi:10.1038/nature01580 Medline
14. D. O. Onwuli, P. Beltran-Alvarez, An update on transcriptional and post-translational regulation of brain voltage-gated sodium channels. *Amino Acids* **48**, 641–651 (2016). doi:10.1007/s00726-015-2122-y Medline
15. D. Ren, B. Navarro, H. Xu, L. Yue, Q. Shi, D. E. Clapham, A prokaryotic voltage-gated sodium channel. *Science* **294**, 2372–2375 (2001). doi:10.1126/science.1065635 Medline
16. D. A. Doyle, J. Morais Cabral, R. A. Pfuetzner, A. Kuo, J. M. Gulbis, S. L. Cohen, B. T. Chait, R. MacKinnon, The structure of the potassium channel: Molecular basis of K⁺ conduction and selectivity. *Science* **280**, 69–77 (1998). doi:10.1126/science.280.5360.69 Medline
17. J. Payandeh, T. Scheuer, N. Zheng, W. A. Catterall, The crystal structure of a voltage-gated sodium channel. *Nature* **475**, 353–358 (2011). doi:10.1038/nature10238 Medline
18. J. Wu, Z. Yan, Z. Li, C. Yan, S. Lu, M. Dong, N. Yan, Structure of the voltage-gated calcium channel Cav1.1 complex. *Science* **350**, aad2395 (2015). doi:10.1126/science.aad2395 Medline
19. L. Yue, B. Navarro, D. Ren, A. Ramos, D. E. Clapham, The cation selectivity filter of the bacterial sodium channel, NaChBac. *J. Gen. Physiol.* **120**, 845–853 (2002). doi:10.1085/jgp.20028699 Medline
20. J. Yang, P. T. Ellinor, W. A. Sather, J. F. Zhang, R. W. Tsien, Molecular determinants of Ca²⁺ selectivity and ion permeation in L-type Ca²⁺ channels. *Nature* **366**, 158–161 (1993). doi:10.1038/366158a0 Medline
21. P. T. Ellinor, J. Yang, W. A. Sather, J. F. Zhang, R. W. Tsien, Ca²⁺ channel selectivity at a single locus for high-affinity Ca²⁺ interactions. *Neuron* **15**, 1121–1132 (1995). doi:10.1016/0896-6273(95)90100-0 Medline
22. I. Favre, E. Moczydowski, L. Schild, On the structural basis for ionic selectivity among Na⁺, K⁺, and Ca²⁺ in the voltage-gated sodium channel. *Biophys. J.* **71**, 3110–3125 (1996). doi:10.1016/S0006-3495(96)79505-X Medline
23. Y. M. Sun, I. Favre, L. Schild, E. Moczydowski, On the structural basis for size-selective permeation of organic cations through the voltage-gated sodium channel. Effect of alanine mutations at the DEKA locus on selectivity, inhibition by Ca²⁺ and H⁺, and molecular sieving. *J. Gen. Physiol.* **110**, 693–715 (1997). doi:10.1085/jgp.110.6.693 Medline
24. C. M. Armstrong, F. Bezanilla, Charge movement associated with the opening and closing of the activation gates of the Na channels. *J. Gen. Physiol.* **63**, 533–552 (1974). doi:10.1085/jgp.63.5.533 Medline
25. N. E. Schoppa, K. McCormack, M. A. Tanouye, F. J. Sigworth, The size of gating charge in wild-type and mutant Shaker potassium channels. *Science* **255**, 1712–1715 (1992). doi:10.1126/science.1553560 Medline
26. S. A. Seoh, D. Sigg, D. M. Papazian, F. Bezanilla, Voltage-sensing residues in the S2 and S4 segments of the Shaker K⁺ channel. *Neuron* **16**, 1159–1167 (1996). doi:10.1016/S0896-6273(00)80142-7 Medline
27. S. K. Aggarwal, R. MacKinnon, Contribution of the S4 segment to gating charge in the Shaker K⁺ channel. *Neuron* **16**, 1169–1177 (1996). doi:10.1016/S0896-6273(00)80143-9 Medline
28. P. G. DeCaen, V. Yarov-Yarovoy, Y. Zhao, T. Scheuer, W. A. Catterall, Disulfide locking a sodium channel voltage sensor reveals ion pair formation during activation. *Proc. Natl. Acad. Sci. U.S.A.* **105**, 15142–15147 (2008). doi:10.1073/pnas.0806486105 Medline
29. P. G. DeCaen, V. Yarov-Yarovoy, E. M. Sharp, T. Scheuer, W. A. Catterall, Sequential formation of ion pairs during activation of a sodium channel voltage sensor. *Proc. Natl. Acad. Sci. U.S.A.* **106**, 22498–22503 (2009). doi:10.1073/pnas.0912307106 Medline
30. X. Zhang, W. Ren, P. DeCaen, C. Yan, X. Tao, L. Tang, J. Wang, K. Hasegawa, T. Kumasaka, J. He, J. Wang, D. E. Clapham, N. Yan, Crystal structure of an orthologue of the NaChBac voltage-gated sodium channel. *Nature* **486**, 130–134 (2012). Medline
31. X. Tao, A. Lee, W. Limapichat, D. A. Dougherty, R. MacKinnon, A gating charge transfer center in voltage sensors. *Science* **328**, 67–73 (2010). doi:10.1126/science.1185954 Medline
32. S. B. Long, E. B. Campbell, R. Mackinnon, Voltage sensor of Kv1.2: Structural basis of electromechanical coupling. *Science* **309**, 903–908 (2005). doi:10.1126/science.1116270 Medline
33. J. R. Whicher, R. MacKinnon, Structure of the voltage-gated K⁺ channel Eag1 reveals an alternative voltage sensing mechanism. *Science* **353**, 664–669 (2016). doi:10.1126/science.aaf8070 Medline
34. C. H. Lee, R. MacKinnon, Structures of the Human HCN1 hyperpolarization-activated channel. *Cell* **168**, 111–120.e11 (2017). doi:10.1016/j.cell.2016.12.023 Medline
35. R. K. Hite, X. Tao, R. MacKinnon, Structural basis for gating the high-conductance Ca²⁺-activated K⁺ channel. *Nature* **541**, 52–57 (2017). doi:10.1038/nature20775 Medline
36. M. Li, X. Zhou, S. Wang, I. Michailidis, Y. Gong, D. Su, H. Li, X. Li, J. Yang, Structure of a eukaryotic cyclic-nucleotide-gated channel. *Nature* **542**, 60–65 (2017). doi:10.1038/nature20819 Medline
37. P. M. Vassilev, T. Scheuer, W. A. Catterall, Identification of an intracellular peptide segment involved in sodium channel inactivation. *Science* **241**, 1658–1661 (1988). doi:10.1126/science.2458625 Medline
38. W. Ulbricht, Sodium channel inactivation: Molecular determinants and modulation. *Physiol. Rev.* **85**, 1271–1301 (2005). doi:10.1152/physrev.00024.2004 Medline
39. G. Yellen, D. Sodickson, T. Y. Chen, M. E. Jurman, An engineered cysteine in the external mouth of a K⁺ channel allows inactivation to be modulated by metal binding. *Biophys. J.* **66**, 1068–1075 (1994). doi:10.1016/S0006-3495(94)80888-4 Medline
40. E. M. Ogielska, W. N. Zagotta, T. Hoshi, S. H. Heinemann, J. Haab, R. W. Aldrich, Cooperative subunit interactions in C-type inactivation of K channels. *Biophys. J.* **69**, 2449–2457 (1995). doi:10.1016/S0006-3495(95)80114-1 Medline
41. H. Todt, S. C. Dudley Jr., J. W. Kyle, R. J. French, H. A. Fozard, Ultra-slow inactivation in mu1 Na⁺ channels is produced by a structural rearrangement of the outer vestibule. *Biophys. J.* **76**, 1335–1345 (1999). doi:10.1016/S0006-3495(99)77296-6 Medline
42. E. Pavlov, C. Bladen, R. Winkfein, C. Diao, P. Dhaliwal, R. J. French, The pore, not cytoplasmic domains, underlies inactivation in a prokaryotic sodium channel. *Biophys. J.* **89**, 232–242 (2005). doi:10.1529/biophysj.104.056994 Medline
43. L. G. Cuello, V. Jogini, D. M. Cortes, E. Perozo, Structural mechanism of C-type inactivation in K⁺ channels. *Nature* **466**, 203–208 (2010). doi:10.1038/nature09153 Medline
44. S. B. Long, X. Tao, E. B. Campbell, R. MacKinnon, Atomic structure of a voltage-dependent K⁺ channel in a lipid membrane-like environment. *Nature* **450**, 376–382 (2007). doi:10.1038/nature06265 Medline
45. E. C. McCusker, C. Bagnérés, C. E. Naylor, A. R. Cole, N. D'Avanzo, C. G. Nichols, B. A. Wallace, Structure of a bacterial voltage-gated sodium channel pore reveals mechanisms of opening and closing. *Nat. Commun.* **3**, 1102 (2012). doi:10.1038/ncomms2077 Medline
46. M. Liao, E. Cao, D. Julius, Y. Cheng, Structure of the TRPV1 ion channel determined by electron cryo-microscopy. *Nature* **504**, 107–112 (2013). doi:10.1038/nature12822 Medline
47. P. Lu, X. C. Bai, D. Ma, T. Xie, C. Yan, L. Sun, G. Yang, Y. Zhao, R. Zhou, S. H. W. Scheres, Y. Shi, Three-dimensional structure of human γ-secretase. *Nature* **512**, 166–170 (2014). doi:10.1038/nature13567 Medline
48. C. Yan, J. Hang, R. Wan, M. Huang, C. C. L. Wong, Y. Shi, Structure of a yeast spliceosome at 3.6-angstrom resolution. *Science* **349**, 1182–1191 (2015). doi:10.1126/science.aac7629 Medline
49. J. Wu, Z. Yan, Z. Li, X. Qian, S. Lu, M. Dong, Q. Zhou, N. Yan, Structure of the voltage-gated calcium channel Cav1.1 at 3.6 Å resolution. *Nature* **537**, 191–196 (2016). doi:10.1038/nature19321 Medline

50. W. Huang, M. Liu, F. S. Yan, N. Yan, Structure-based assessment of disease-related mutations in human voltage-gated sodium channels. *Protein Cell* **2017**, s13238-017-0372-z (2017). doi:10.1007/s13238-017-0372-z
51. D. Slowik, R. Henderson, Benchmarking the stability of human detergent-solubilised voltage-gated sodium channels for structural studies using eel as a reference. *Biochim. Biophys. Acta* **1848**, 1545–1551 (2015). doi:10.1016/j.bbamem.2015.03.021 Medline
52. K. Dong, Insect sodium channels and insecticide resistance. *Invert. Neurosci.* **7**, 17–30 (2007). doi:10.1007/s10158-006-0036-9 Medline
53. G. Feng, P. Déák, M. Chopra, L. M. Hall, Cloning and functional analysis of TipE, a novel membrane protein that enhances *Drosophila para* sodium channel function. *Cell* **82**, 1001–1011 (1995). doi:10.1016/0092-8674(95)90279-1 Medline
54. B. Moignot, C. Lemaire, S. Quinchard, B. Lapiède, C. Legros, The discovery of a novel sodium channel in the cockroach *Periplaneta americana*: Evidence for an early duplication of the para-like gene. *Insect Biochem. Mol. Biol.* **39**, 814–823 (2009). doi:10.1016/j.ibmb.2009.09.006 Medline
55. J. W. West, D. E. Patton, T. Scheuer, Y. Wang, A. L. Goldin, W. A. Catterall, A cluster of hydrophobic amino acid residues required for fast Na⁺-channel inactivation. *Proc. Natl. Acad. Sci. U.S.A.* **89**, 10910–10914 (1992). doi:10.1073/pnas.89.22.10910 Medline
56. P. S. Shen, X. Yang, P. G. DeCaen, X. Liu, D. Bulkley, D. E. Clapham, E. Cao, The structure of the polycystic kidney disease channel PKD2 in lipid nanodiscs. *Cell* **167**, 763–773.e11 (2016). doi:10.1016/j.cell.2016.09.048 Medline
57. C. M. Bourdin, B. Moignot, L. Wang, L. Murillo, M. Juchaux, S. Quinchard, B. Lapiède, N. C. Guérineau, K. Dong, C. Legros, Intron retention in mRNA encoding ancillary subunit of insect voltage-gated sodium channel modulates channel expression, gating regulation and drug sensitivity. *PLOS ONE* **8**, e67290 (2013). doi:10.1371/journal.pone.0067290 Medline
58. R. K. Finol-Urdaneta, Y. Wang, A. Al-Sabi, C. Zhao, S. Y. Noskov, R. J. French, Sodium channel selectivity and conduction: Prokaryotes have devised their own molecular strategy. *J. Gen. Physiol.* **143**, 157–171 (2014). doi:10.1085/jgp.201311037 Medline
59. B. Hille, The permeability of the sodium channel to organic cations in myelinated nerve. *J. Gen. Physiol.* **58**, 599–619 (1971). doi:10.1085/jgp.58.6.599 Medline
60. S. Das, J. Gilchrist, F. Bosmans, F. Van Petegem, Binary architecture of the Nav1.2-β2 signaling complex. *eLife* **5**, 10.7554/eLife.10960 (2016). doi:10.7554/elife.10960 Medline
61. C. M. Armstrong, F. Bezanilla, Currents related to movement of the gating particles of the sodium channels. *Nature* **242**, 459–461 (1973). doi:10.1038/242459a0 Medline
62. W. Stühmer, F. Conti, H. Suzuki, X. D. Wang, M. Noda, N. Yahagi, H. Kubo, S. Numa, Structural parts involved in activation and inactivation of the sodium channel. *Nature* **339**, 597–603 (1989). doi:10.1038/339597a0 Medline
63. P. Vassilev, T. Scheuer, W. A. Catterall, Inhibition of inactivation of single sodium channels by a site-directed antibody. *Proc. Natl. Acad. Sci. U.S.A.* **86**, 8147–8151 (1989). doi:10.1073/pnas.86.20.8147 Medline
64. C. A. Rohl, F. A. Boeckman, C. Baker, T. Scheuer, W. A. Catterall, R. E. Klevit, Solution structure of the sodium channel inactivation gate. *Biochemistry* **38**, 855–861 (1999). doi:10.1021/bi9823380 Medline
65. C. Wang, B. C. Chung, H. Yan, S. Y. Lee, G. S. Pitt, Crystal structure of the ternary complex of a NaV C-terminal domain, a fibroblast growth factor homologous factor, and calmodulin. *Structure* **20**, 1167–1176 (2012). doi:10.1016/j.str.2012.05.001 Medline
66. D. L. Capes, M. P. Goldschen-Ohm, M. Arcisio-Miranda, F. Bezanilla, B. Chanda, Domain IV voltage-sensor movement is both sufficient and rate limiting for fast inactivation in sodium channels. *J. Gen. Physiol.* **142**, 101–112 (2013). doi:10.1085/jgp.201310998 Medline
67. B. Chanda, F. Bezanilla, Tracking voltage-dependent conformational changes in skeletal muscle sodium channel during activation. *J. Gen. Physiol.* **120**, 629–645 (2002). doi:10.1085/jgp.20028679 Medline
68. M. P. Goldschen-Ohm, D. L. Capes, K. M. Oelstrom, B. Chanda, Multiple pore conformations driven by asynchronous movements of voltage sensors in a eukaryotic sodium channel. *Nat. Commun.* **4**, 1350 (2013). doi:10.1038/ncomms2356 Medline
69. H. K. Motoike, H. Liu, I. W. Glaaser, A.-S. Yang, M. Tateyama, R. S. Kass, The Na⁺ channel inactivation gate is a molecular complex: A novel role of the COOH-terminal domain. *J. Gen. Physiol.* **123**, 155–165 (2004). doi:10.1085/jgp.200308929 Medline
70. R. S. Kass, Sodium channel inactivation in heart: A novel role of the carboxy-terminal domain. *J. Cardiovasc. Electrophysiol.* **17** (Suppl 1), S21–S25 (2006). doi:10.1111/j.1540-8167.2006.00381.x Medline
71. S. Ahuja, S. Mukund, L. Deng, K. Khakh, E. Chang, H. Ho, S. Shriver, C. Young, S. Lin, J. P. Johnson Jr., P. Wu, J. Li, M. Coons, C. Tam, B. Brillantes, H. Sampang, K. Mortara, K. K. Bowman, K. R. Clark, A. Estevez, Z. Xie, H. Verschoof, M. Grimwood, C. Dehnhardt, J.-C. Andrez, T. Focken, D. P. Sutherlin, B. S. Safina, M. A. Starovasnik, D. F. Ortwin, Y. Franke, C. J. Cohen, D. H. Hackos, C. M. Koth, J. Payandeh, Structural basis of Nav1.7 inhibition by an isoform-selective small-molecule antagonist. *Science* **350**, aac5464 (2015). doi:10.1126/science.aac5464 Medline
72. S. Y. Wang, G. K. Wang, A mutation in segment I-S6 alters slow inactivation of sodium channels. *Biophys. J.* **72**, 1633–1640 (1997). doi:10.1016/S0006-3495(97)78809-X Medline
73. V. Yarov-Yarovoy, J. C. McPhee, D. Idsvoog, C. Pate, T. Scheuer, W. A. Catterall, Role of amino acid residues in transmembrane segments IS6 and IIS6 of the Na⁺ channel alpha subunit in voltage-dependent gating and drug block. *J. Biol. Chem.* **277**, 35393–35401 (2002). doi:10.1074/jbc.M206126200 Medline
74. Y. Chen, F. H. Yu, D. J. Surmeier, T. Scheuer, W. A. Catterall, Neuromodulation of Na⁺ channel slow inactivation via cAMP-dependent protein kinase and protein kinase C. *Neuron* **49**, 409–420 (2006). doi:10.1016/j.neuron.2006.01.009 Medline
75. G. M. Lipkind, H. A. Fozard, Molecular modeling of local anesthetic drug binding by voltage-gated sodium channels. *Mol. Pharmacol.* **68**, 1611–1622 (2005). Medline
76. C. A. Ahern, A. L. Eastwood, D. A. Dougherty, R. Horn, Electrostatic contributions of aromatic residues in the local anesthetic receptor of voltage-gated sodium channels. *Circ. Res.* **102**, 86–94 (2008). doi:10.1161/CIRCRESAHA.107.160663 Medline
77. T. Matsuda, C. L. Cepko, Electroporation and RNA interference in the rodent retina in vivo and in vitro. *Proc. Natl. Acad. Sci. U.S.A.* **101**, 16–22 (2004). doi:10.1073/pnas.2235688100 Medline
78. X. Li, P. Mooney, S. Zheng, C. R. Booth, M. B. Braunfeld, S. Gubbens, D. A. Agard, Y. Cheng, Electron counting and beam-induced motion correction enable near-atomic-resolution single-particle cryo-EM. *Nat. Methods* **10**, 584–590 (2013). doi:10.1038/nmeth.2472 Medline
79. S. Zheng, E. Palovcak, J.-P. Armache, Y. Cheng, D. Agard, Anisotropic correction of beam-induced motion for improved single-particle electron cryo-microscopy. *bioRxiv*, 10.1101/061960 (2016). <https://doi.org/10.1101/061960>
80. T. Grant, N. Grigorieff, Measuring the optimal exposure for single particle cryo-EM using a 2.6 Å reconstruction of rotavirus VP6. *eLife* **4**, e06980 (2015). doi:10.7554/elife.06980 Medline
81. K. Zhang, Gctf: Real-time CTF determination and correction. *J. Struct. Biol.* **193**, 1–12 (2016). doi:10.1016/j.jsb.2015.11.003 Medline
82. S. H. Scheres, Semi-automated selection of cryo-EM particles in RELION-1.3. *J. Struct. Biol.* **189**, 114–122 (2015). doi:10.1016/j.jsb.2014.11.010 Medline
83. S. H. Scheres, A Bayesian view on cryo-EM structure determination. *J. Mol. Biol.* **415**, 406–418 (2012). doi:10.1016/j.jmb.2011.11.010 Medline
84. S. H. Scheres, RELION: Implementation of a Bayesian approach to cryo-EM structure determination. *J. Struct. Biol.* **180**, 519–530 (2012). doi:10.1016/j.jsb.2012.09.006 Medline
85. D. Kimanius, B. O. Forsberg, S. H. Scheres, E. Lindahl, Accelerated cryo-EM structure determination with parallelisation using GPUs in RELION-2. *eLife* **5**, 10.7554/eLife.18722 (2016). doi:10.7554/elife.18722 Medline
86. T. Grant, N. Grigorieff, Automatic estimation and correction of anisotropic magnification distortion in electron microscopes. *J. Struct. Biol.* **192**, 204–208 (2015). doi:10.1016/j.jsb.2015.08.006 Medline
87. X. Gong, H. Qian, X. Zhou, J. Wu, T. Wan, P. Cao, W. Huang, X. Zhao, X. Wang, P. Wang, Y. Shi, G. F. Gao, Q. Zhou, N. Yan, Structural insights into the Niemann-Pick C1 (NPC1)-mediated cholesterol transfer and Ebola infection. *Cell* **165**, 1467–1478 (2016). doi:10.1016/j.cell.2016.05.022 Medline

88. P. B. Rosenthal, R. Henderson, Optimal determination of particle orientation, absolute hand, and contrast loss in single-particle electron cryomicroscopy. *J. Mol. Biol.* **333**, 721–745 (2003). doi:10.1016/j.jmb.2003.07.013 Medline
89. S. Chen, G. McMullan, A. R. Faruqi, G. N. Murshudov, J. M. Short, S. H. W. Scheres, R. Henderson, High-resolution noise substitution to measure overfitting and validate resolution in 3D structure determination by single particle electron cryomicroscopy. *Ultramicroscopy* **135**, 24–35 (2013). doi:10.1016/j.ultramic.2013.06.004 Medline
90. N. Stein, CHAINSAW: A program for mutating pdb files used as templates in molecular replacement. *J. Appl. Cryst.* **41**, 641–643 (2008). doi:10.1107/S0021889808006985
91. P. Emsley, B. Lohkamp, W. G. Scott, K. Cowtan, Features and development of Coot. *Acta Crystallogr. D Biol. Crystallogr.* **66**, 486–501 (2010). doi:10.1107/S0907444910007493 Medline
92. P. D. Adams, P. V. Afonine, G. Bunkóczki, V. B. Chen, I. W. Davis, N. Echols, J. J. Headd, L.-W. Hung, G. J. Kapral, R. W. Grosse-Kunstleve, A. J. McCoy, N. W. Moriarty, R. Oeffner, R. J. Read, D. C. Richardson, J. S. Richardson, T. C. Terwilliger, P. H. Zwart, PHENIX: A comprehensive Python-based system for macromolecular structure solution. *Acta Crystallogr. D Biol. Crystallogr.* **66**, 213–221 (2010). doi:10.1107/S0907444909052925 Medline
93. G. N. Murshudov, P. Skubák, A. A. Lebedev, N. S. Pannu, R. A. Steiner, R. A. Nicholls, M. D. Winn, F. Long, A. A. Vagin, REFMAC5 for the refinement of macromolecular crystal structures. *Acta Crystallogr. D Biol. Crystallogr.* **67**, 355–367 (2011). doi:10.1107/S0907444911001314 Medline
94. R. A. Nicholls, M. Fischer, S. McNicholas, G. N. Murshudov, Conformation-independent structural comparison of macromolecules with ProSMART. *Acta Crystallogr. D Biol. Crystallogr.* **70**, 2487–2499 (2014). doi:10.1107/S1399004714016241 Medline
95. A. Amunts, A. Brown, X. C. Bai, J. L. Llacer, T. Hussain, P. Emsley, F. Long, G. Murshudov, S. H. W. Scheres, V. Ramakrishnan, Structure of the yeast mitochondrial large ribosomal subunit. *Science* **343**, 1485–1489 (2014). doi:10.1126/science.1249410 Medline
96. O. Goldenberg, E. Erez, G. Nimrod, N. Ben-Tal, The ConSurf-DB: Pre-calculated evolutionary conservation profiles of protein structures. *Nucleic Acids Res.* **37** (Database), D323–D327 (2009). doi:10.1093/nar/gkn822 Medline
97. E. F. Pettersen, T. D. Goddard, C. C. Huang, G. S. Couch, D. M. Greenblatt, E. C. Meng, T. E. Ferrin, UCSF Chimera—a visualization system for exploratory research and analysis. *J. Comput. Chem.* **25**, 1605–1612 (2004). doi:10.1002/jcc.20084 Medline
98. W. L. DeLano, The PyMOL Molecular Graphics System; <http://www.pymol.org> (2002).
99. O. S. Smart, J. G. Neduvilil, X. Wang, B. A. Wallace, M. S. Sansom, HOLE: A program for the analysis of the pore dimensions of ion channel structural models. *J. Mol. Graph.* **14**, 354–360, 376 (1996). doi:10.1016/S0263-7855(97)00009-X Medline
100. M. Biasini, S. Bienert, A. Waterhouse, K. Arnold, G. Studer, T. Schmidt, F. Kiefer, T. Gallo Cassarino, M. Bertoni, L. Bordoli, T. Schwede, SWISS-MODEL: Modelling protein tertiary and quaternary structure using evolutionary information. *Nucleic Acids Res.* **42** (W1), W252–W258 (2014). doi:10.1093/nar/gku340 Medline
101. K. Arnold, L. Bordoli, J. Kopp, T. Schwede, The SWISS-MODEL workspace: A web-based environment for protein structure homology modelling. *Bioinformatics* **22**, 195–201 (2006). doi:10.1093/bioinformatics/bti770 Medline
102. N. Guex, M. C. Peitsch, T. Schwede, Automated comparative protein structure modeling with SWISS-MODEL and Swiss-PdbViewer: A historical perspective. *Electrophoresis* **30** (Suppl 1), S162–S173 (2009). doi:10.1002/elps.200900140 Medline
103. F. Kiefer, K. Arnold, M. Künzli, L. Bordoli, T. Schwede, The SWISS-MODEL Repository and associated resources. *Nucleic Acids Res.* **37** (Database), D387–D392 (2009). doi:10.1093/nar/gkn750 Medline
104. A. T. Brünger, P. D. Adams, G. M. Clore, W. L. DeLano, P. Gros, R. W. Grosse-Kunstleve, J. S. Jiang, J. Kuszewski, M. Nilges, N. S. Pannu, R. J. Read, L. M. Rice, T. Simonson, G. L. Warren, Crystallography & NMR system: A new software suite for macromolecular structure determination. *Acta Crystallogr. D Biol. Crystallogr.* **54**, 905–921 (1998). doi:10.1107/S090744498003254 Medline
105. A. T. Brunger, Version 1.2 of the crystallography and NMR system. *Nat. Protoc.* **2**, 2728–2733 (2007). doi:10.1038/nprot.2007.406 Medline

ACKNOWLEDGMENTS

We thank Jianlin Lei, Xiaomei Li, and Xiaomin Li for technical support during EM image acquisition. We thank Kun Wu, Jiaofeng Chen, Shuai Fu, Xuechen Zhu, Hai Qi, Wei Xiong, Bailong Xiao, Cecilia Canessa, and Qinghua Tao at Tsinghua University for technical support and critical discussions. We thank the Tsinghua University Branch of China National Center for Protein Sciences (Beijing) for providing the cryo-EM facility support. We thank the computational facility support on the cluster of Bio-Computing Platform (Tsinghua University Branch of China National Center for Protein Sciences Beijing) and the “Explorer 100” cluster system of Tsinghua National Laboratory for Information Science and Technology. This work was supported by funds from the Ministry of Science and Technology of China (2015CB910101, 2016YFA0500402, 2014ZX09507003-006) and the National Natural Science Foundation of China (projects 31621092, 31630017, and 31611130036). N.Y. was supported in part by an International Early Career Scientist grant from the Howard Hughes Medical Institute and an endowed professorship from Bayer Healthcare. The atomic coordinates have been deposited in the Protein Data Bank with the accession code 5XOM and the EM map has been deposited in EMDB with accession code EMD-6698.

SUPPLEMENTARY MATERIALS

www.sciencemag.org/cgi/content/full/science.aa14326/DC1
Figs. S1 to S10
Table S1
References

18 November 2016; accepted 31 January 2017

Published online 9 February 2017

10.1126/science.aa14326

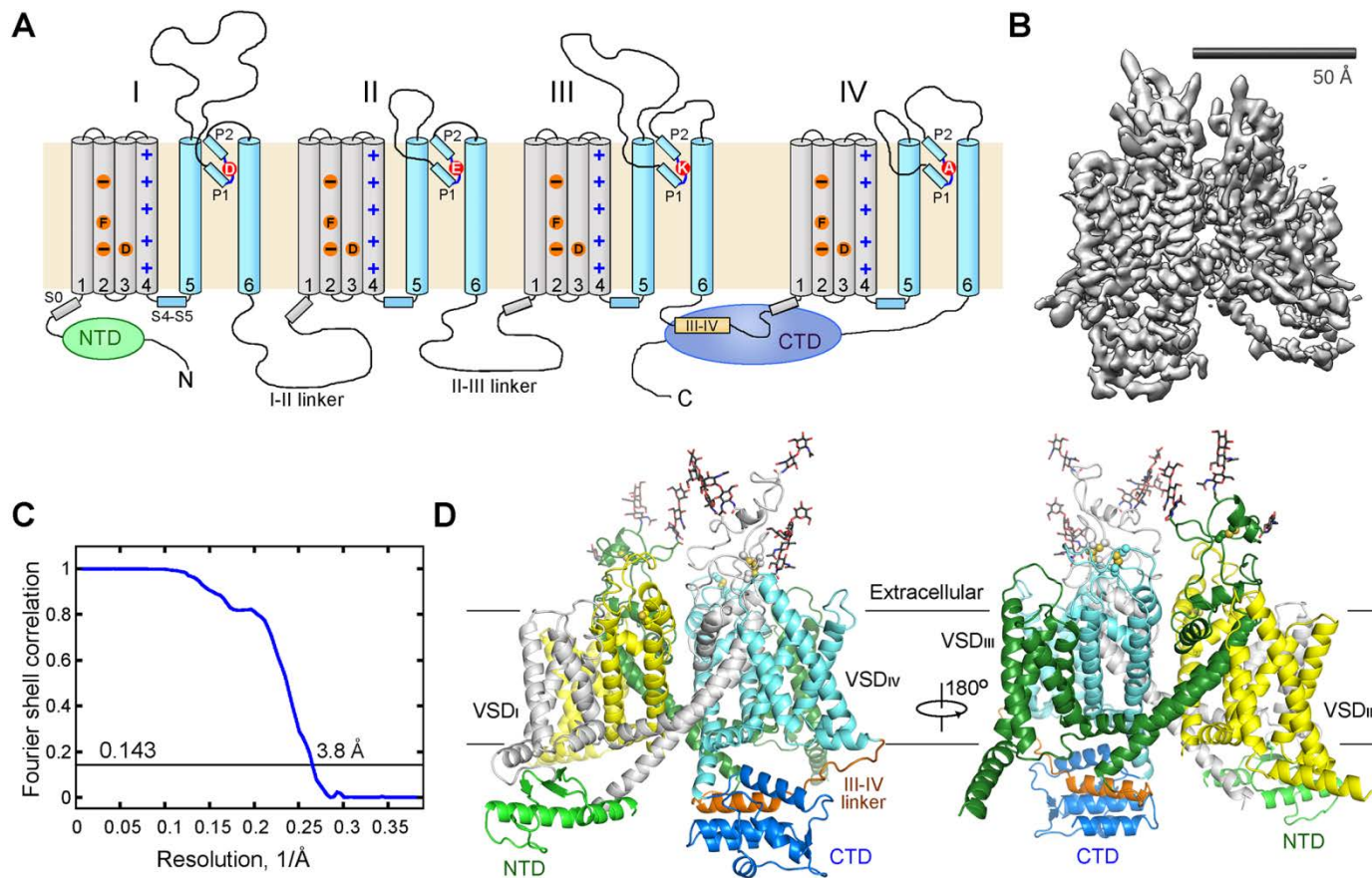


Fig. 1. The structure of Na_vPaS determined using single particle cryo-EM. (A) The general topology of eukaryotic Na_v channels. The previously identified key residues in ion selectivity and voltage-sensing are indicated. “F” represents cyclic hydrophobic residues that occlude the gating charges from either side of the membrane. “-” represents the negative or polar residues on S2 segments that are designated An1 and An2. **(B)** The EM reconstruction of Na_vPaS . The map was generated in Chimera (97). **(C)** The Gold-standard Fourier shell correlation (FSC) curve for the 3D reconstruction of the EM map. **(D)** The overall structure of Na_vPaS . The structure is domain colored. The glycosyl moieties and disulfide bonds are shown as sticks and spheres, respectively. All structure figures were prepared in PyMol (98).

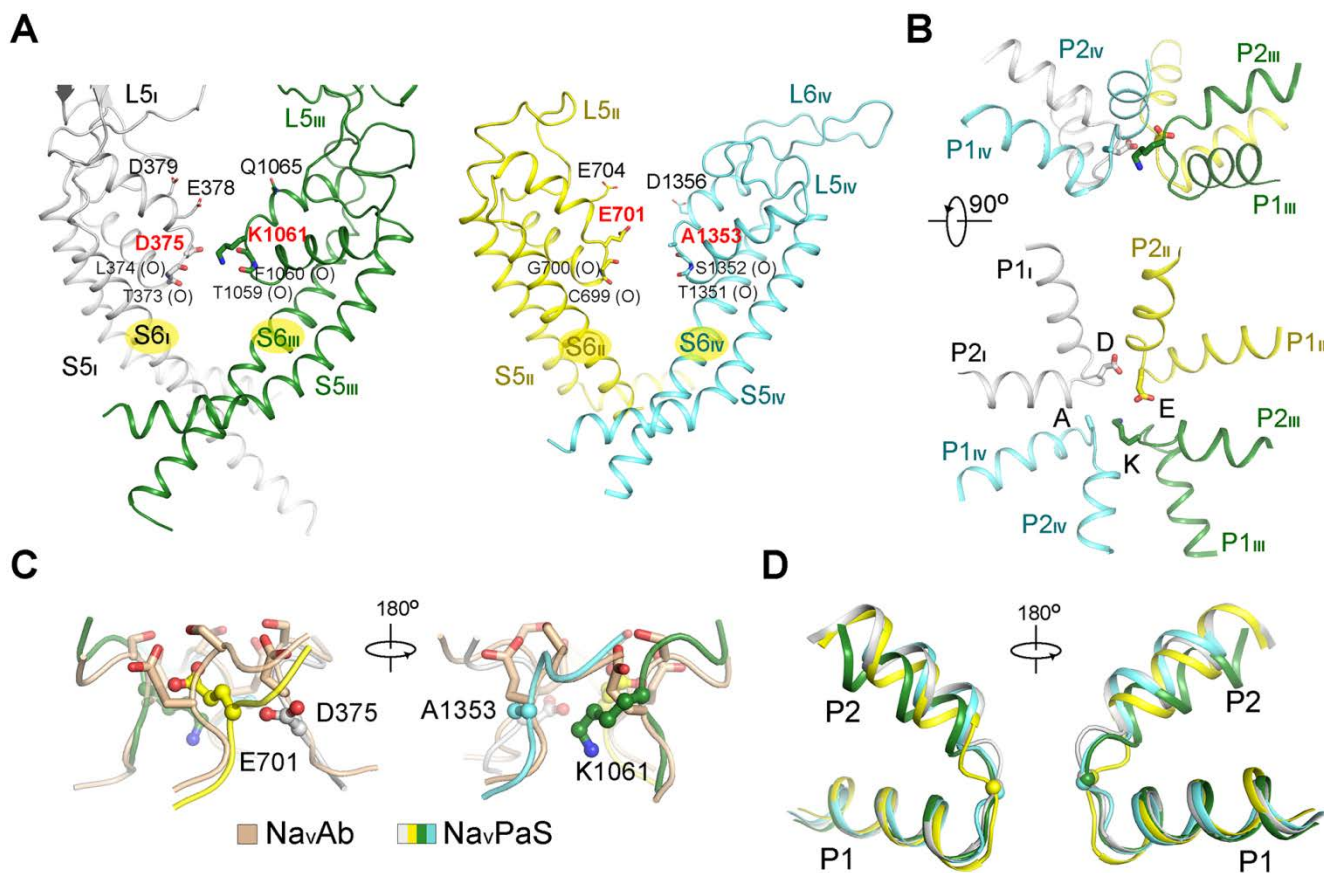


Fig. 2. The asymmetric selectivity filter (SF) of NaPaS. (A) The SF vestibule is enclosed by the side groups of Asp/Glu/Lys/Ala (DEKA) and the carbonyl oxygen atoms of the two preceding residues in each repeat. The residues that constitute the negative ring above the SF vestibule are also shown. (B) Structure of the signature DEKA residues that are critical for Na⁺ selectivity. Two perpendicular views are shown. (C) Structural variations of the selectivity filter between one-chain NaPaS and homotetrameric NaAb. Whereas the inner site constituted by the carbonyl oxygen groups remain similar, the outer site formed by the side groups of DEKA in NaPaS is distinct from that formed by Ser/Glu in NaAb (PDB code: 3RVY) with respect to both chemical composition and structural conformation. (D) The deviated backbone conformations of the SF sequences in the four repeats. The SF sequence in repeat II (yellow) is one residue shorter than those in the other three. The superimposed SF sequences and pore helices P1 and P2 in the four repeats are presented in two opposite side views. The C_α atoms of DEKA are shown as spheres.

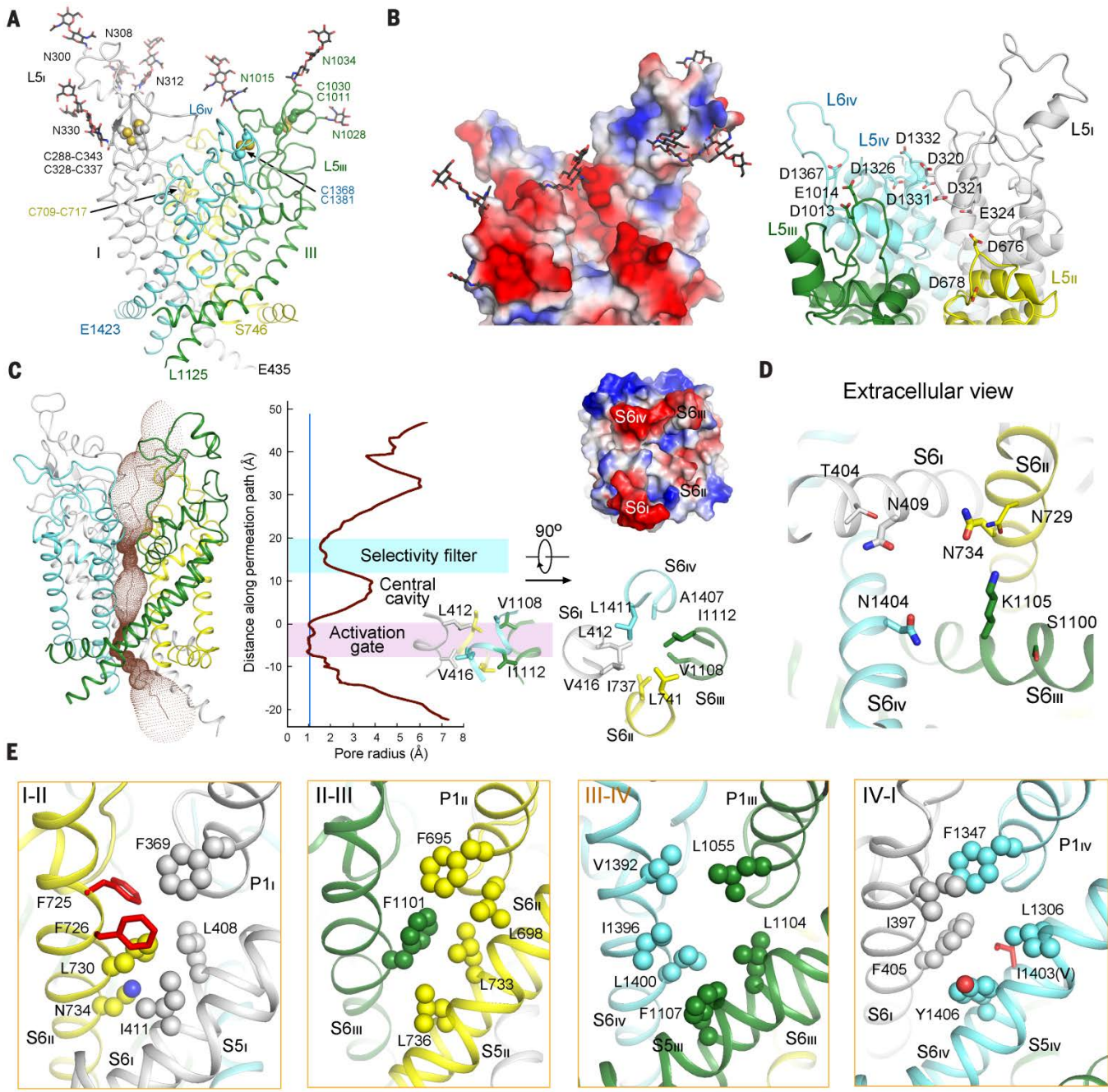


Fig. 3. A closed pore with only one narrow fenestration. (A) The heavily glycosylated extracellular loops above the pore domain are stabilized by multiple disulfide bonds. (B) The extracellular loops provide the electronegative potential surrounding the outer mouth to the SF vestibule. The surface electrostatic potential was calculated in PyMol. (C) The intracellular gate is closed. The permeation path, calculated by HOLE (99), is illustrated by brown dots in the left panel. The pore radii along the conducting passage are tabulated in the middle panel. The two layers of the hydrophobic residues that form the intracellular gate are shown as sticks in two perpendicular views. A bottom view of surface electrostatic potential of the pore domain is shown in the upper panel. (D) The polar and charged residues within the central cavity of the pore domain. An extracellular view is shown. The highly conserved Asn409/Asn734/Lys1105/Asn1404 residues at corresponding locus on S6 point to the central cavity in the current conformation. Please refer to fig. S1 for detailed sequence comparison and fig. S7B for side views of the central cavity. (E) The pore domain is sealed from the lipid bilayer except for a small fenestration enclosed by the S6 segments in repeats III and IV. The residues that seal the central cavity from the lipid bilayer are shown, with the invariant ones between Na_vPaS and human Na_v channels as spheres and the altered ones as red sticks.

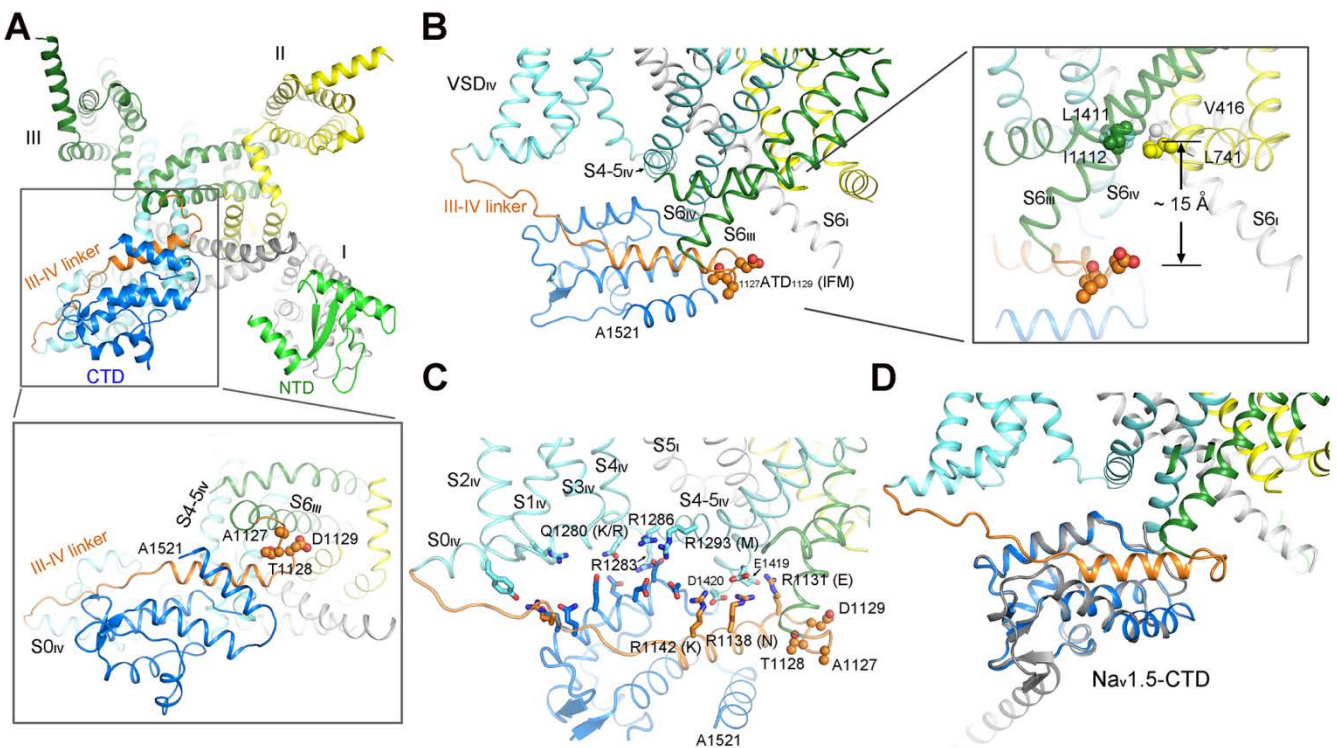


Fig. 4. Extensive interactions between the III-IV linker, CTD and adjacent structural elements. (A) The α helix-containing III-IV linker interacts with the globular CTD. An enlarged view of the III-IV linker, the CTD, and the adjacent pore-forming segments are shown in the inset. Residues Ala/Thr/Asp (ATD), which correspond to the fast inactivation motif IMF, are shown as spheres. (B) The IFM motif-corresponding residues are located on a turn connecting S6_{III} and the III-IV helix. Inset: The ATD motif is distanced from the lower layer of the intracellular gate by approximately 15 Å. (C) Extensive interactions between the III-IV linker, CTD, VSD_{IV}, S4-S5_{IV} and S6_{IV}. The polar and charged residues that may contribute to the interactions are shown as sticks. The corresponding residues in human Na_v channels, if different from those in Na_vPaS, are annotated in bracket. (D) Na_vPaS-CTD is structurally similar to Na_v1.5-CTD. The structures of Na_vPaS-CTD and Na_v1.5-CTD (PDB code: 4DCK) can be superimposed with a root-mean-square deviation of 0.318 Å over 71 C α atoms.

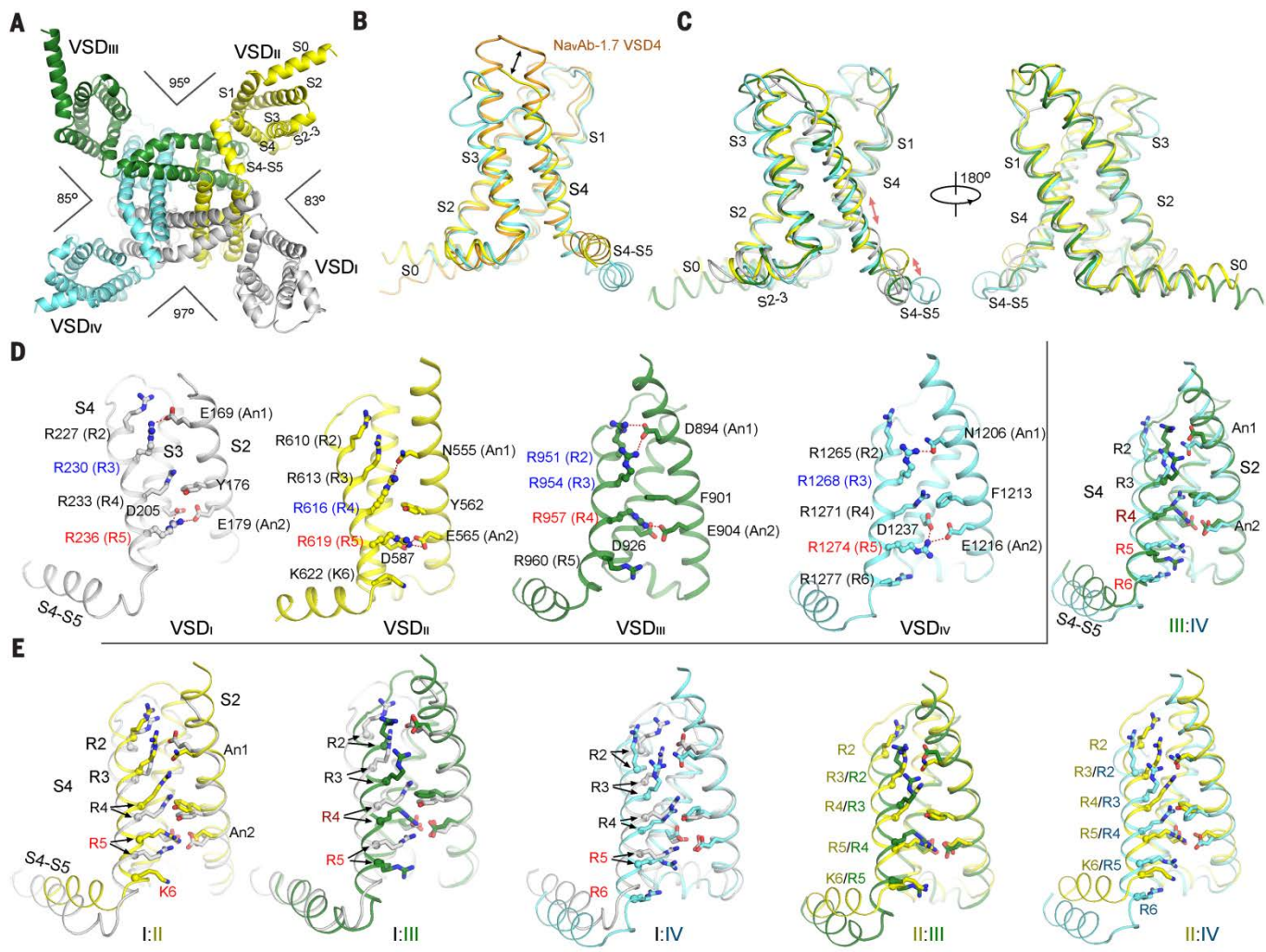


Fig. 5. The four VSDs of Na_vPaS exhibit distinct conformational states. (A) All four VSDs are completely resolved. A bottom view is shown with the intracellular segments omitted for visual clarity. The relative angles between neighboring VSDs are estimated in Chimera, wherein the respective and common centroids of the VSDs are determined and the relative angles are calculated based on the distances between these centroids. (B) The Na_vPaS-VSDs have shorter S3 and S4 segments than the chimeric Na_vAb-1.7 VSD4. The structural comparison is made between VSD_{II} and VSD_{IV} of Na_vPaS with Na_vAb-1.7 VSD4 (PDB code: 5EK0). (C) The four VSDs exhibit distinct conformations. The four VSD structures are superimposed relative to the charge transfer center (CTC) and An1 on S2. The same reference is used for all the domain comparisons shown in this figure. The shifts of the backbone of S4 and the ensuing S4-S5 linker are indicated by red arrows. Two opposite side views are shown. (D) Structures of the Na_vPaS-VSDs. For visual clarity, the S1 segment in each VSD is omitted. The side chains of the gating charges on S4, the CTC residues (An2 and the occluding Phe/Tyr on S2, and a conserved Asp on S3), and An1 are shown. The gating charge residues that are coordinated by An1 and An2 are labeled blue and red, respectively. (E) Pairwise comparison of the VSDs. The C_α atoms of the gating charge residues are shown as spheres.

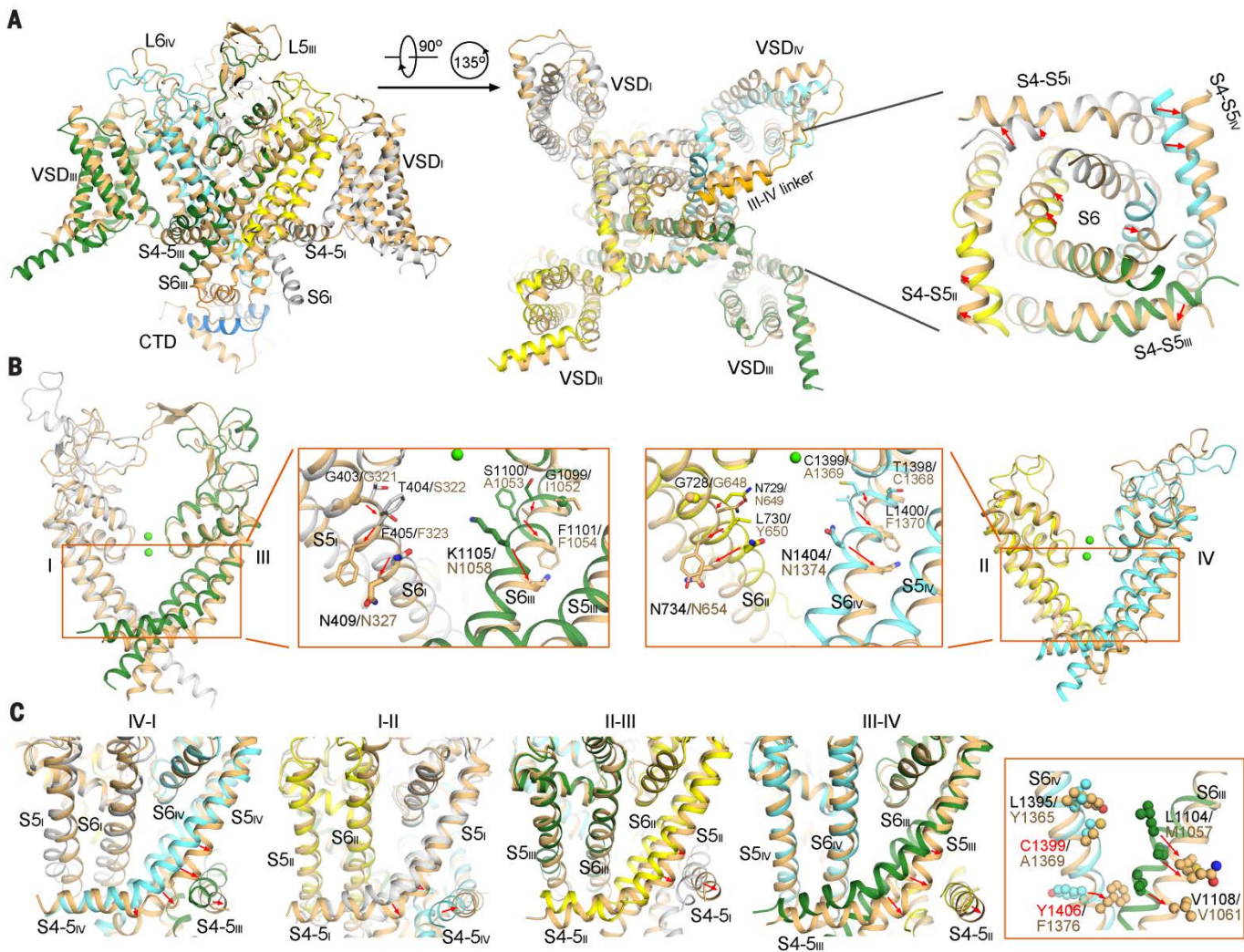


Fig. 6. Structural changes between Na_vPaS and Ca_v1.1. (A) Comparison of the overall structures of Na_vPaS and Ca_v1.1 (PDB code: 5GJV, chain A). The structures are superimposed relative to the funnel constituted by the P1-SF-P2 segments in the four repeats. The CTDs are omitted in the intracellular view. Right panel: The S4-S5 constriction ring appears to be relaxed from Na_vPaS to Ca_v1.1. The red arrows indicate the shifts of the corresponding structural elements from Na_vPaS to Ca_v1.1 in the intracellular view. (B) The S6 segments undergo axial rotation between Na_vPaS and Ca_v1.1, placing the conserved Asn residues inside or outside the central cavity of the pore domain, respectively. Structural alignment suggests that the rotations initiate at the G(S/T)F motif or corresponding positions on S6. (C) Structural shifts of S5 and S6 are coupled to the opening or closure of the fenestrations. Inset: the corresponding residues that are involved in the binding of local anesthetic drugs adopt distinct conformations in Na_vPaS and Ca_v1.1. The residues Cys1399 and Tyr1406 correspond to Phe1764 and Tyr1771 in Na_v1.2, respectively (75). Please refer to Movies 1 to 3 for detailed analysis of the conformational changes between Na_vPaS and Ca_v1.1.

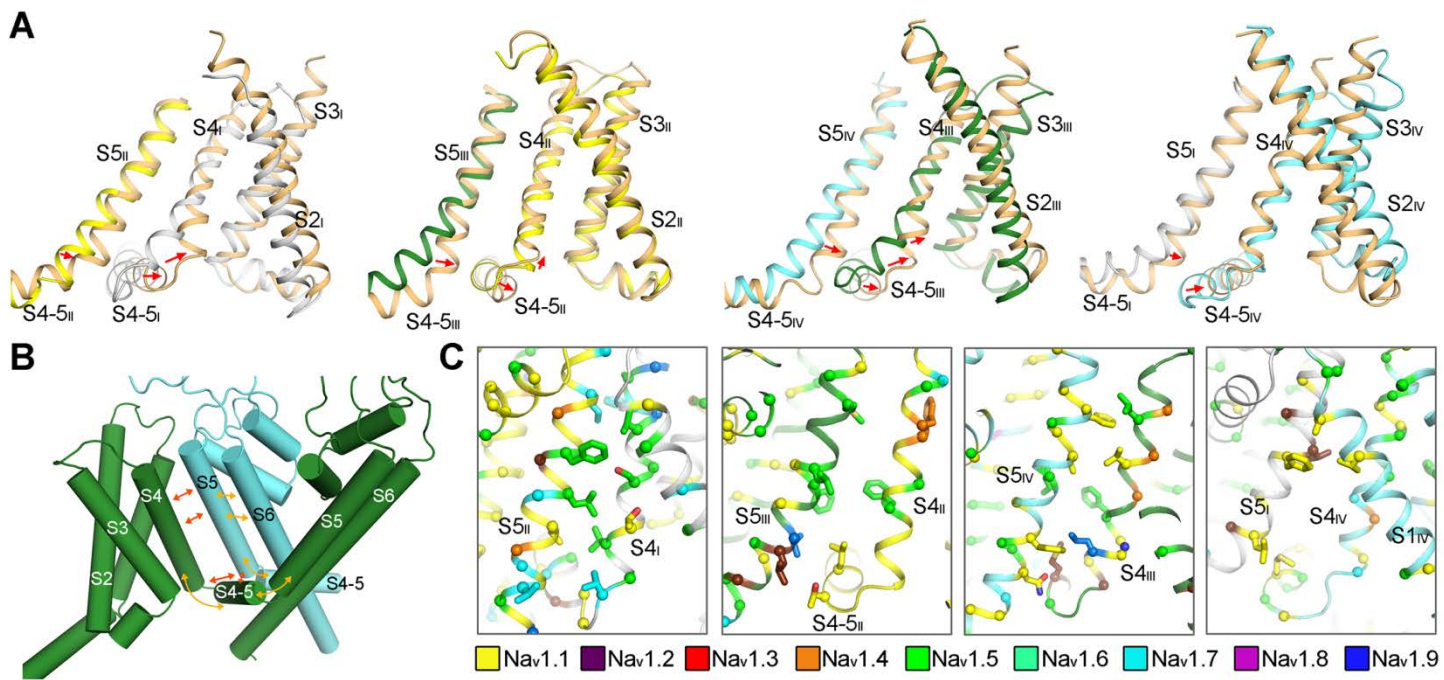


Fig. 7. Implications on the electromechanical coupling mechanism of Na_v and Ca_v channels. (A) The conformational changes of the corresponding VSDs and neighboring S5 segments between Na_vPaS and Ca_v1.1. The two structures are superimposed as in Fig. 6A. The red arrows indicate the shifts of the corresponding segments from Na_vPaS to Ca_v1.1. (B) The electromechanical coupling of voltage-gated ion channels with “canonical” fold may involve intricate and extensive interactions between adjacent S4, S4-S5, S5, and S6 segments in the same and neighboring repeats. The potential interactions that are responsible for coupled motions between intra- and inter-repeat elements are indicated by orange and red arrows, respectively. (C) A number of disease-related mutations of Na_v channels mapped to the interface between S4 and S5 segments in the neighboring repeats. The C_α atoms of representative disease-related residues are shown as spheres and the interface residues are shown as sticks. The residues are color-coded for the Na_v subtypes in which the mutations were identified (50). When mutations occur to the same locus in different channels, the one in the channel with higher number is shown. Please refer to Movies 4 and 5 for the conformational changes illustrated in this figure.

Movie 1. The overall structural changes between Na_vPaS and Ca_v1.1. A homologous model of Na_vPaS derived from the structure of Ca_v1.1 was generated based on sequence alignment in fig. S8 using SWISS-MODEL webserver (<https://www.swissmodel.expasy.org>) (100–103). The modeled structure was superimposed to the cryo-EM structure of Na_vPaS relative to the selectivity filter and the P1 and P2 helices (the P1-SF-P2 funnel). The cryo-EM structure of Na_vPaS and the homologous structural model of Na_vPaS were used as the initial and end frame, respectively, for morph generation. The intermediate morphs were generated using the Crystallography and NMR System (CNS) (104, 105). The movies were prepared in PyMOL. The NTD and extracellular loops are omitted. The structures are domain-colored following the same scheme as in Fig. 1D.

Movie 2. Conformational changes of the pore domain segments between Na_vPaS and Ca_v1.1. An intracellular view is shown. The conserved Asn/Lys residues on the S6 segments are shown as sticks. The axial rotations of S6 segments between the two structures result in the placement of the conserved Asn/Lys residues inside or outside the central cavity.

Movie 3. The structural shifts of S5 and S6 segments lead to the opening or closure of fenestrations. The pore domain is shown as cartoon under semi-transparent surface. The S6_{III} and S6_{IV} residues corresponding to those in Na_v1.2 and Na_v1.4 that may be involved in binding to local anesthetics are shown as spheres (75, 76).

Movie 4. Coupled motions between VSDs and pore domain elements. The shifts of S4 and S4-S5 linker in one repeat appear to be coupled to the concerted motion of S5 and S6 in the neighboring repeat.

Movie 5. Representative disease-related mutations mapped to the interface between S4 and S5 segments in the adjacent repeats. It is noted that the interfaces between S4_I and S5_{II} and between S4_{III} and S5_{IV} host more disease mutations than those between S4_{II} and S5_{III} and between S4_{IV} and S5_I.



Structure of a eukaryotic voltage-gated sodium channel at near-atomic resolution
Huaizong Shen, Qiang Zhou, Xiaojing Pan, Zhangqiang Li, Jianping Wu
and Nieng Yan (February 9, 2017)
published online February 9, 2017

Editor's Summary

This copy is for your personal, non-commercial use only.

- Article Tools** Visit the online version of this article to access the personalization and article tools:
<http://science.sciencemag.org/content/early/2017/02/08/science.aal4326>
- Permissions** Obtain information about reproducing this article:
<http://www.sciencemag.org/about/permissions.dtl>

Science (print ISSN 0036-8075; online ISSN 1095-9203) is published weekly, except the last week in December, by the American Association for the Advancement of Science, 1200 New York Avenue NW, Washington, DC 20005. Copyright 2016 by the American Association for the Advancement of Science; all rights reserved. The title *Science* is a registered trademark of AAAS.